Comparative study of the ferromagnetic resonance behavior of coupled rectangular and circular $Ni_{80}Fe_{20}$ rings

G. Shimon,[1,2] A. O. Adeyeye,[1,2,*] and C. A. Ross[2,3,†]

[1]*Department of Electrical and Computer Engineering, 4 Engineering Drive 3, National University of Singapore, Singapore 117576, Singapore*

[2]*Singapore-MIT Alliance, 4 Engineering Drive 3, Singapore 117576, Singapore*

[3]*Department of Materials Science and Engineering, Massachusetts Institute of Technology, Cambridge, MA 02139, USA*

(Received 23 September 2013; revised manuscript received 29 November 2013; published 7 January 2014)

A systematic investigation of the dynamic behavior of $Ni_{80}Fe_{20}$ ring arrays using broadband ferromagnetic resonance spectroscopy as a function of inter-ring spacing and ring thickness is presented. Four distinct resonance modes were found for rectangular rings compared to the two modes seen in circular rings of identical width due to the presence of sharp corners and nonuniform demagnetization field distribution. The resonance peaks were sensitive to the inter-ring spacing and the ring thickness due to magnetostatic coupling. Micromagnetic simulations and analytical calculations are compared with the experiment results.

DOI: 10.1103/PhysRevB.89.024302 PACS number(s): 75.75.−c, 76.50.+g, 75.78.Cd

I. INTRODUCTION

The investigation of dynamic behavior in ferromagnetic patterned elements is important in designing high-frequency memory elements [1,2], logic devices [3–5], and tunable magnonic filters [6,7]. Ferromagnetic rings are particularly interesting because they show a range of magnetic states at remanence such as the onion (or bi-domain) state, with two 180° domain walls (DWs), and the vortex (flux-closed) state, depending on the reversal process and the ring dimensions. To date, there are many reports on the static behavior of magnetic rings including circular [8–10], elliptical [11], triangular [12,13], square [14,15], rhombic [16], rounded rectangular [17,18], and rectangular rings [19]. The effect of ring dimensions [20–22], shapes [19,23], inter-ring spacing [24,25], configurational anisotropy [11,26,27], and engineered defects [28,29] on static reversal of the rings have also been examined. In contrast, reports on dynamic behavior of ring elements have focused on the investigation of circular ring [30–33] and limited work on other ring shapes such as rounded rectangular [34] and triangular rings [35].

It is well known that the large demagnetizing fields associated with the boundaries of elements affect their magnetic configuration and switching mechanism. In circular rings, the boundaries of the structure as well as inhomogeneous internal fields become the source of spin wave confinement [36] and determine whether spin wave propagation is allowed or forbidden. In nanowires and nanostrips, the existence of bends and kinks also introduces nonuniform internal fields that can change the character of propagating spin waves or act as a propagation barrier [37]. Correspondingly, the sharp 90° corners in square or rectangular rings can become barriers to a propagating spin wave, in addition to trapping DWs [19,38]. A comparison between the dynamic behavior of a rectangular ring with sharp corners and a circular ring is useful in providing model structures to study spin wave confinement and the effect of shape anisotropy on dynamic behavior of ring arrays. Furthermore, an investigation of their packing density is important in designing compact spin wave guides [39] and tunable magnonic filters [6].

In this paper, we compare the dynamic behavior of narrow rectangular $Ni_{80}Fe_{20}$ (NiFe) rings with sharp corners with those of circular rings. Using broadband ferromagnetic resonance (FMR) spectroscopy, four resonance modes were found in rectangular rings instead of two resonance modes in circular rings. The corners of rectangular rings are responsible for the detection of one of the additional modes. Another mode is observed due to the nonuniform demagnetizing field in the hard-axis arms of rectangular rings, which causes two modes to exist instead of the one found for circular rings. The ring shape affects not only the number of resonance modes but also frequency values by modifying the anisotropy field and demagnetizing field in different sections of the rings. We also investigated the effect of magnetostatic interactions as a function of inter-ring spacing s for varying ring thickness t. The effect of shape anisotropy and the dynamic interaction between neighboring rings on the high-frequency response of ring array will be useful in the design of magnonic crystal devices based on arrays of patterned magnetic elements.

II. EXPERIMENTAL DETAILS

The arrays of NiFe rectangular and circular rings were fabricated on a silicon substrate using deep ultraviolet lithography at 248-nm exposure wavelength and electron beam evaporation followed by a liftoff process. Details of the fabrication process were described previously [40]. NiFe rings with t in the range of 30 nm to 120 nm were deposited at a rate of 0.2 Å/s with a base pressure of 4×10^{-8} Torr. The liftoff was determined visually by a contrast change in the patterned film during the process and was confirmed using scanning electron microscopy (SEM). Figure 1 presents SEM micrographs of rectangular and circular ring arrays with a well-defined edge profile. The rectangular rings had an outer edge dimension of 5 μm × 3 μm, while the circular rings had an outer diameter of 3 μm. The ring width for both shapes was fixed at 350 nm. The inter-ring spacing s was varied from s = 550 nm to s = 150 nm.

*Corresponding author: eleaao@nus.edu.sg
†caross@mit.edu

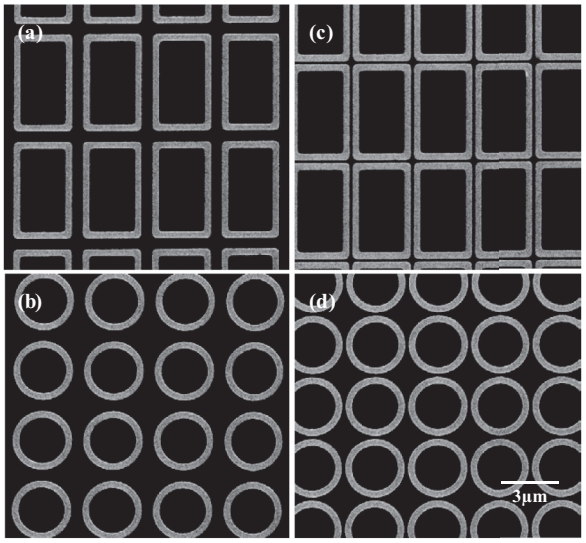

FIG. 1. SEM micrographs of (a), (b) further apart (spacing, s = 550 nm) and (c), (d) closely spaced (s = 150 nm) rectangular and circular rings arrays.

To excite and detect FMR of a ring array, a ground-signal-ground (G-S-G)-type coplanar waveguide (CPW) was fabricated on top of it using photolithography and deposition of an Al_2O_3(50 nm)/Ti(5 nm)/Au(200 nm) stack. The FMR response of the nanostructures was measured using a microwave vector network analyzer connected to the CPWs using G-S-G-type microwave coplanar probes [35]. The FMR response was measured at room temperature by sweeping the frequency for fixed applied field (H_{app}) in the 1–20 GHz range. This process was repeated for a series of H_{app} values starting from a negative saturation field (H_{sat}) of −1400 Oe to a positive saturation of 1400 Oe. A reference signal was taken at negative saturation $H_{sat} = -1400$ Oe prior to the actual sample measurement to subtract the background noise from the measurement.

Micromagnetic simulations were performed using the LLG Micromagnetics Simulator™ [41]. The saturation magnetization was taken as $M_{s,\mathrm{NiFe}} = 860$ emu cm^{-3}, exchange constant $A_{\mathrm{NiFe}} = 13 \times 10^{-7}$ erg cm^{-1}, and magnetocrystalline anisotropy $K_{1,\mathrm{NiFe}} = 0$. A unit cell size of 10 nm × 10 nm × 10 nm thickness was used in the simulations. A simulation using a smaller cell, 5 nm × 5 nm × 10 nm, gave similar results. The masks used in the simulations were extracted from SEM images of the fabricated structures. To simulate the FMR response and quantify the spatial characteristics of different resonance modes, time-dependent simulations were performed using a gyromagnetic ratio $\frac{\gamma}{2\pi} = 2.8$ GHz/kOe and $\alpha = 0.008$. The dynamic simulation results were analyzed in the frequency domain by performing Fast Fourier Transform processing.

III. RESULTS AND DISCUSSION

A. Arrays with inter-element separation of 550 nm

Figures 2(a) and (b) show the two-dimensional (2D) FMR absorption spectra plots for t = 30 nm and s = 550 nm rectangular and circular rings, respectively. The overlapping symbol plots are the corresponding simulated FMR peaks for single rings. The number of modes and the trends in the resonance peak versus interring spacing agree well with the experiments. We observed four resonance modes in rectangular rings and two resonance modes in circular rings. Common to both rings are the resonance in the sides of the rings oriented parallel to H_{app} [easy axis mode **A**; Figs. 2(f), 2(l)] and perpendicular to H_{app} [hard axis mode **B**; Figs. 2(g), 2(m)]. Mode **A** undergoes a splitting when a vortex state is formed, i.e., for 125 Oe < H_{app} < 330 Oe for the rectangular ring and 95 Oe < H_{app} < 420 Oe for circular ring. The splitting occurs due to the two opposite magnetization directions in each ring arm when a vortex is formed, i.e., one parallel and one antiparallel to the H_{app} direction. The former exhibits a negative dispersion in resonance frequency ($df_{res}/dH < 0$), while the latter exhibits a positive dispersion ($df_{res}/dH > 0$) [42]. These modes have been identified in circular rings previously [30].

Another two modes, labeled **C** and **D**, were observed only in rectangular rings. Mode **C** is an edge mode in the short arms of the rectangular ring [Fig. 2(h)] occurring at higher fields. In rectangular rings, there is a strong maximum H_{demag} along the edge of the short arms [see Fig. 3(b)], which causes mode **C** to have a lower resonance frequency of 6.15 GHz at 1400 Oe (near saturation) compared to mode **B**. This observation is similar to the case of the hard-axis edge response in a triangular ring [35]. Mode **C** was not observed in circular rings due to a broader H_{demag} distribution in the curved arms [compare Figs. 3(b) and 3(d)]. Mode **D** is the resonance mode around the 180° DWs (180DW), which occur in the straight sides of the rings, and the 90° DWs (90DW), which occur at the corners [see Figs. 2(i) and 2(j)]. Mode **D** has a low intensity but appears around −700 Oe < H_{app} < −300 Oe in experiment, a field range in which 180DW and 90DW are expected to be present. Figure 2(j) shows these walls in a simulation at 400 Oe. The sharp corners in the rectangular ring provide locations for 90DW at moderate field values [19,43].

From the 2D-FMR spectra, we observed that $f_{\mathbf{A}} > f_{\mathbf{B}}$ for both ring shapes at all H_{app} values. The resonance peaks of t = 30 nm rings at $H_{sat} = -1400$ Oe are shown in Figs. 2(c) and 2(d). For rectangular rings $f_{\mathbf{A}} = 13.17$ GHz and $f_{\mathbf{B}} = 7.64$ GHz, while for circular rings $f_{\mathbf{A}} = 12.88$ GHz and $f_{\mathbf{B}} = 8.02$ GHz. The resonance frequencies of modes **A** and **B** can be explained using the Kittel formula below. This is done by considering only a specific section of a ring's arm in the saturated state and estimating the effect of ring shape and neighboring interaction as the modifying factor(s) in the formula:

$$f_{\mathrm{res}} = \frac{\gamma}{2\pi}\sqrt{(H_{\mathrm{eff}} + (N_z - N_y)M_y)(H_{\mathrm{eff}} + (N_x - N_y)M_y)}, \quad (1)$$

where N_x, N_y, and N_z are the demagnetizing factors for x, y, and thickness (z) directions, respectively; $N_x + N_y + N_z = 4\pi$, γ is the gyromagnetic ratio; M_y is the magnetization of the sample along H_{app}, i.e., along the y direction; and H_{eff} is the effective field in the y direction. In mode **A**, the effective field is enhanced by an anisotropy field (H_{ani}) along the easy-axis

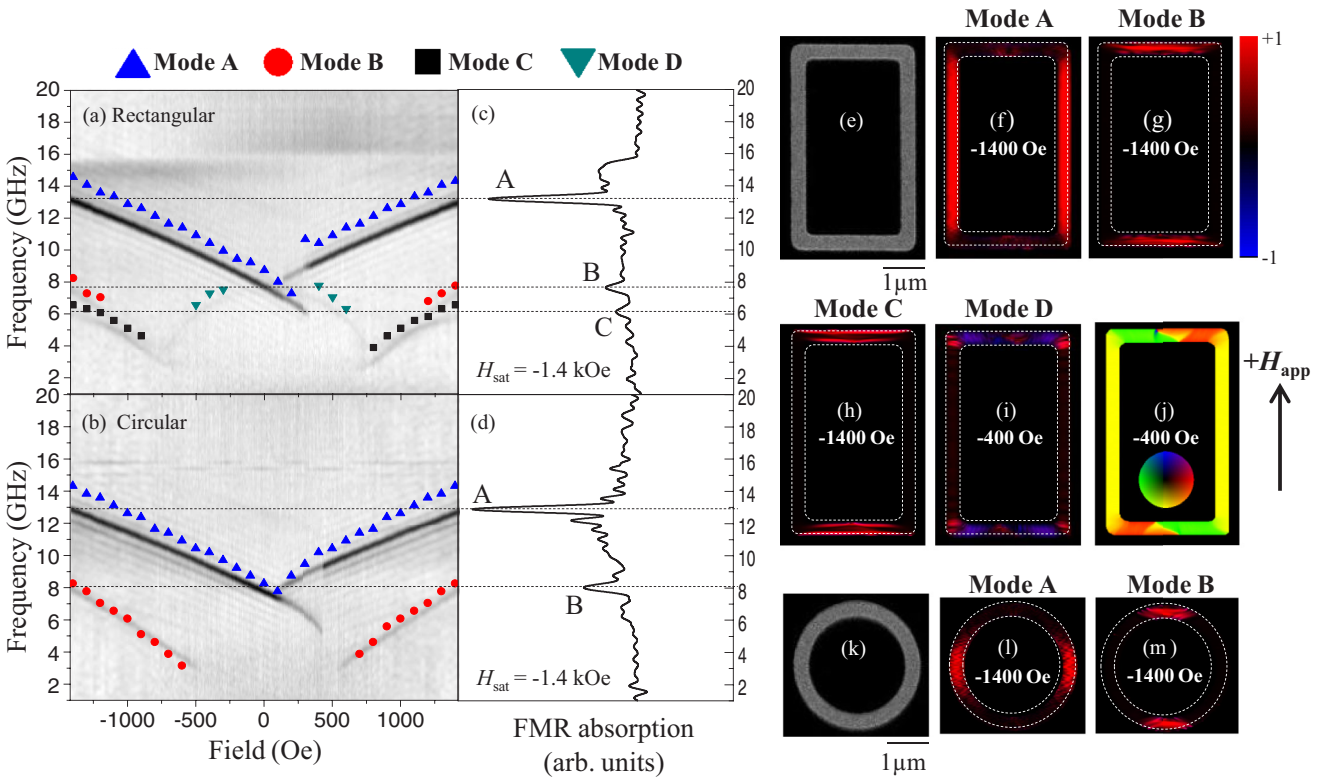

FIG. 2. (Color online) (a), (b) 2D FMR absorption intensity plots of 30-nm-thick film NiFe rings. Plotted symbols are the corresponding simulated FMR frequency. (c), (d) FMR spectrum for each ring shape extracted at $H_{sat} = -1.4$ kOe. (e) SEM micrographs of the rectangular rings. (f)–(h) The simulated mode profiles showing modes **A** to **C** in a rectangular ring at $H_{sat} = -1.4$ kOe. (i)–(j) Simulated mode **D** and its corresponding static DW configuration in a rectangular ring at $H_{app} = -400$ Oe. Inset in (j) shows the color wheel of the magnetization. The color scale bar shows normalized FMR absorption intensity. (k) SEM micrographs of the circular rings. (l), (m) The simulated mode profiles showing modes **A** and **B** in a circular ring at $H_{sat} = -1.4$ kOe.

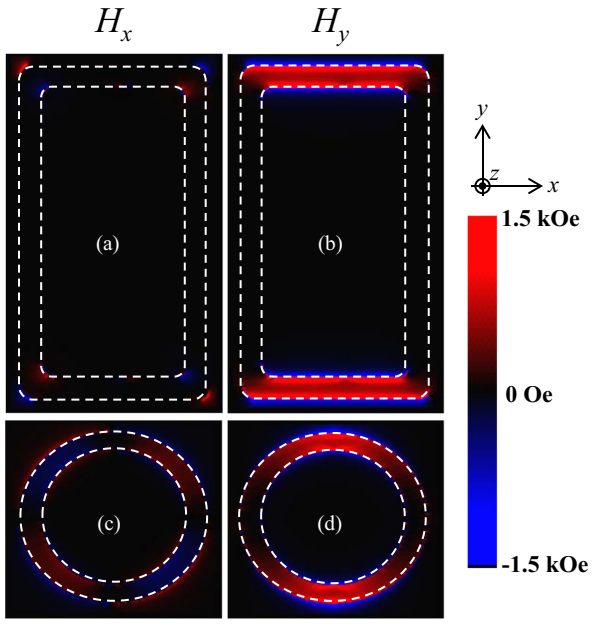

FIG. 3. (Color online) Simulated stray field components (H_x and H_y) at $h = 5$ nm above the surface of (a), (b) rectangular rings and (c), (d) circular rings. Film thickness $t = 30$ nm. Scale bar represents the stray field in Oe. The rings were saturated along y at $H_{sat} = -1.4$ kOe.

direction, i.e., $H_{eff} = H_{app} + H_{ani}$, which produces a larger resonance frequency as compared to mode **B**. In mode **B**, the effective field is reduced by the demagnetization field $|H_{demag}|$ of the hard-axis arms to $H_{eff} = H_{app} - |H_{demag}|$ to yield a lower resonance frequency. Comparing the two ring shapes at saturation, the rectangular ring had a larger $f_{\mathbf{A}}$ by ~290 MHz but a smaller $f_{\mathbf{B}}$ by ~380 MHz compared with circular rings. The higher $f_{\mathbf{A}}$ is attributed to the stronger shape anisotropy (larger H_{ani}) of the rectangular ring along the y direction, while the lower $f_{\mathbf{B}}$ is attributed to the larger $|H_{demag}|$.

B. Interacting ring arrays

In this section, we compare the $f_{\mathbf{A}}$ in rectangular and circular rings as a function of s and t at saturation. Figures 4(a) and 4(b) show FMR spectra of $t = 30$ nm rings at 1400 Oe, while $s = 550$ nm and $s = 150$ nm to show a typical decrease in $f_{\mathbf{A}}$ as s reduces. In this example, for $t = 30$ nm, for the rectangular ring $\Delta f_{\mathbf{A}} = 240$ MHz, while for the circular ring $\Delta f_{\mathbf{A}} = 190$ MHz. The $f_{\mathbf{A}}$ values for the range of 150 nm $\leq s \leq$ 550 nm and 30 nm $\leq t \leq$ 120 nm for both rings' shapes are given in Figs. 4(e) and 4(f). Over the range of t, the same trend of decreasing $f_{\mathbf{A}}$ values occurred as s was reduced, and $\Delta f_{\mathbf{A}}$ was generally larger for rectangular rings than for circular

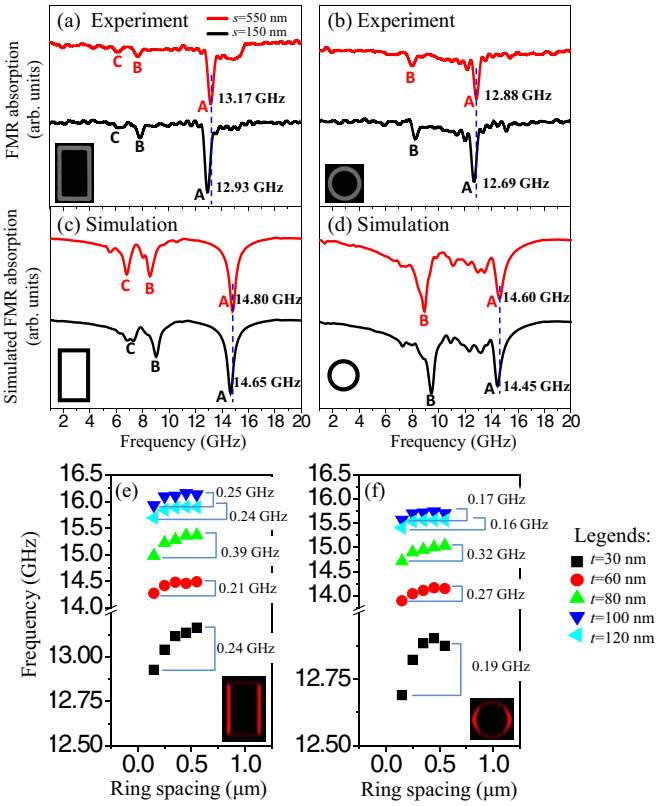

FIG. 4. (Color online) (a), (b) Experimental and (c), (d) Simulated FMR spectra at $H_{sat} = -1.4$ kOe showing a shift in f_A as a function of s for $t = 30$ nm. (e), (f) Extracted FMR frequencies of mode **A** at $H_{sat} = -1.4$ kOe as a function of t and s. Note the scale break in the frequency axis ~14 GHz.

rings. For $t = 80$ nm, Δf_A reaches its maximum value of $\Delta f_A = 390$ MHz for rectangular rings and $\Delta f_A = 320$ MHz for circular rings. f_A reached its maximum value at $t = 100$ nm for all s in both ring shapes.

FMR simulations with 2D periodic boundary condition for $t = 30$ nm were carried out for rectangular and circular rings [Figs. 4(c) and 4(d)]. We found a similar decrease of $\Delta f_A \sim 150$ MHz for both ring shapes when s was reduced from 550 nm to 150 nm. These Δf_A values become larger for $t = 80$ nm rings, with $\Delta f_A = 240$ MHz for rectangular and $\Delta f_A = 200$ MHz for circular rings. These trends are consistent with the experimental results [Figs. 4(e) and 4(f)].

1. The effect of inter-ring spacing

To investigate the decreasing trend of f_A with the reduction of s, we estimate the stray field distribution away from the ring edge using, as an example, 30-nm-thick rings magnetized parallel to y. At height $h = 5$ nm above the ring's surface, there is a stray field in the y direction $|H_y| \sim 1.5$ kOe around the edges of the rings [Figs. 3(b), 3(d)] and also in the x direction $|H_x| \sim 1.5$ kOe at the corners of the rectangular ring [Fig. 3(a)]. These stray fields decrease to a negligible value at ~150 nm away from the edge. The stray fields from one ring affect the f_A of a neighboring ring in two ways: (1) H_y in the direction of the applied field increases $H_{eff} = H_{app} + H_y$; and (2) H_x lowers the effective H_{demag} in x direction and modifies N_x according to $\Delta N_x = \frac{H_x}{M_s}$ and consequently increases N_y and N_z.

To simplify the analysis, one arm of the rectangular ring is treated as a strip magnet [Fig. 5(a)], with normalized stray field adapted from J. Norpoth *et al.* [44],

$$H_x(\text{norm.}) = \ln\left\{\frac{\sqrt{\alpha^2+(z-0.5c)^2}\cdot(\beta+\sqrt{\alpha^2+\beta^2+(z+0.5c)^2})}{\sqrt{\alpha^2+(z+0.5c)^2}\cdot(\beta+\sqrt{\alpha^2+\beta^2+(z-0.5c)^2})}\right\}\Bigg|_{\alpha=x-0.5a}^{\alpha=x+0.5a}\Bigg|_{\beta=y-0.5b}^{\beta=y+0.5b} \quad (2)$$

$$H_y(\text{norm.}) = \frac{1}{4\pi}\times\left\{\arctan\left[\frac{\alpha\cdot\beta}{(z-0.5c)\cdot\sqrt{\alpha^2+\beta^2+(z-0.5c)^2}}\right] - \arctan\left[\frac{\alpha\cdot\beta}{(z+0.5c)\cdot\sqrt{\alpha^2+\beta^2+(z+0.5c)^2}}\right]\right\}\Bigg|_{\alpha=x-0.5a}^{\alpha=x+0.5a}\Bigg|_{\beta=y-0.5b}^{\beta=y+0.5b}. \quad (3)$$

As shown in Fig. 5(b), the width (w), length (l), and t of a strip are along the x, y, and z direction, and the origin is at the body center of the strip such that its boundaries are given as $-0.5a \leqslant x \leqslant 0.5a$, $-0.5c \leqslant y \leqslant 0.5c$ and $-0.5b \leqslant z \leqslant 0.5b$, where $a = w = 350$ nm, $b = t$ nm, and $c = l = 5$ μm.

First, the resonance frequency of an isolated strip was calculated from expressions developed by Aharoni [45] to estimate the demagnetizing factors of the isolated strip. Taking the dimensions of the strip as $w = 350$ nm, $l = 5$ μm, and $t = 30$ nm, the demagnetizing factors were $N_x = 0.424\pi, N_y = 0.028\pi$, and $N_z = 3.548\pi$. Substituting $H_y = -1400$ Oe, $M_s = 860$ emu.cm^{-3}, $\frac{\gamma}{2\pi} = 2.8$ GHz/kOe, and the estimated demagnetizing factors into (1), the resonance frequency of an isolated strip would be 14.54 GHz.

Subsequently, using (2) and (3), the H_x (norm.) $= \frac{H_x}{4\pi M_s}$ and H_y (norm.) $= \frac{H_y}{4\pi M_s}$ at $h = 5$ nm was calculated above the ring's surface (following the numerical simulations), i.e., at $z = (0.5b + 5)$ nm. The 2D stray field profiles are plotted in Figs. 5(c) and 5(d). From Fig. 5(c), it is clear that the majority of the H_x arises from the corners of the strip, similar to the simulated H_x in a rectangular ring [Fig. 4(a)]. H_y is concentrated at the strip's ends [Fig. 5(d)]. The maximum $|H_{x,y}(\text{norm.})|$ was estimated as ~0.2 or a field of ~2.16 kOe, slightly larger than the maxima in simulations.

To give a clearer picture of the stray field distribution, the normalized stray field along the width at $y = 0.501c$ and along the length at $x = 0.5a$ for both x and y directions are shown in Figs. 5(e)–5(h). Based on these plots, we estimated

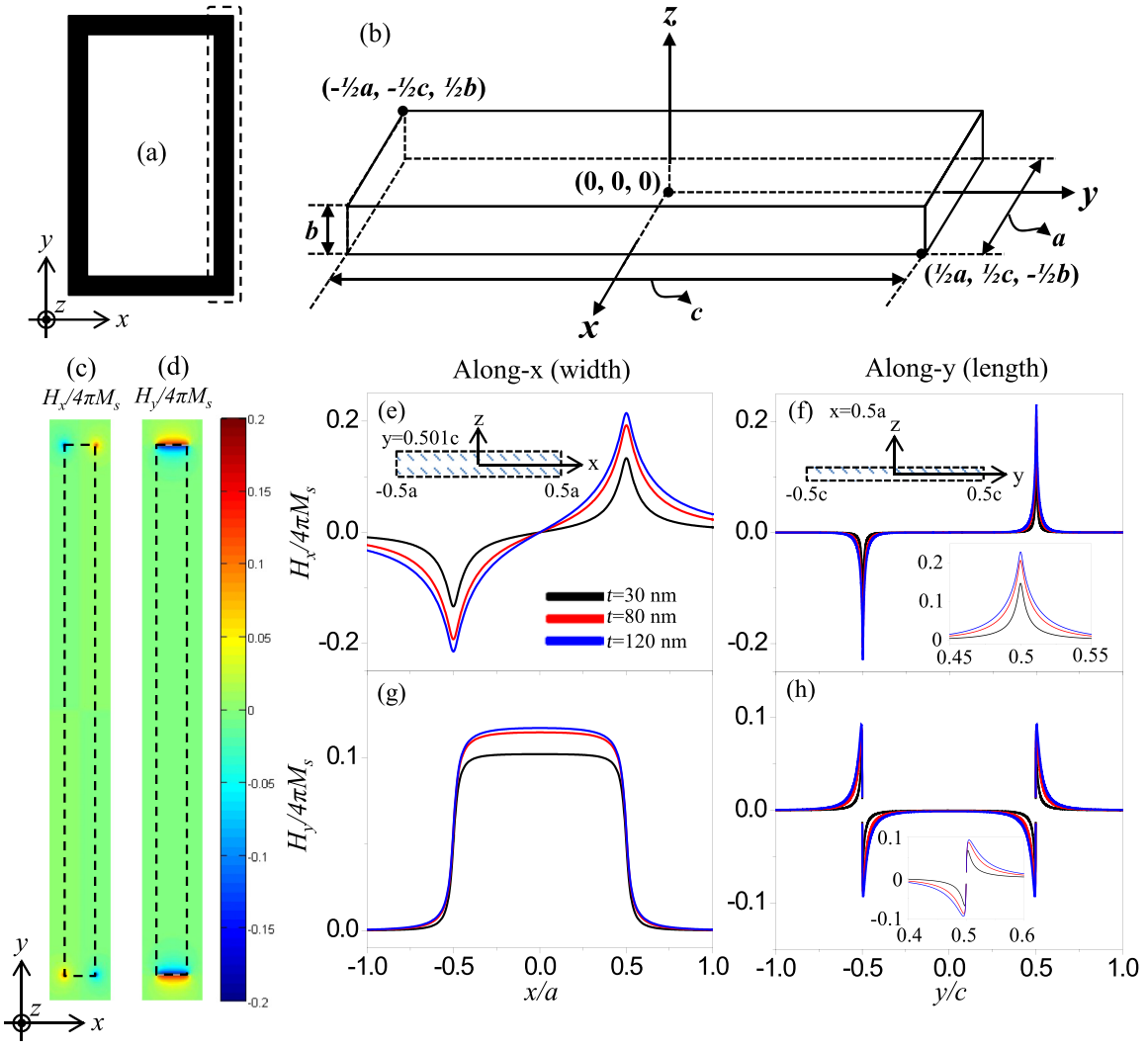

FIG. 5. (Color online) (a), (b) Schematic diagram of strip magnet used in analytical calculation of stray field. Dotted line in (a) highlights the part of the rectangular ring estimated as a strip. (c), (d) The calculated 2D plot of normalized stray field ($H_x/4\pi M_s$ and $H_y/4\pi M_s$) for $t = 30$ nm and $h = 5$ nm. Scale bar indicates the normalized stray field value with respect to $4\pi M_s$. (e)–(h) Plots of normalized stray field calculated at $h = 5$ nm along x ($y = 0.501c$) and along y ($x = 0.5a$) for various film thicknesses.

$H_{x,y}$ (norm.) at a distance $s = 150$ nm away from the strip's edges for $t = 30$ nm. H_y (norm.) was ~0.0143 or about -154 Oe along the strip's length [Fig. 5(h) at $y/c = 0.53$]. Similarly, H_x (norm.) was estimated as ~0.011 or ~118 Oe along the strip's width [Fig. 5(e) at $x/a = 0.93$)]. Then ΔN_x due to H_x was determined as $\Delta N_x = \frac{-H_x}{M_s} = -0.0439\pi$; consequently, $\Delta N_y = |\Delta N_x| \times \frac{N_y}{N_y+N_z} = 3.416 \times 10^{-4}\pi$, and $\Delta N_z = |\Delta N_x| \times \frac{N_z}{N_y+N_z} = 0.0436\pi$.

The stray field $H_y = -154$ Oe would be expected to raise the resonance frequency to 15.09 GHz or $\Delta f_{\text{res}} = 550$ MHz according to Eq. (1). This is inconsistent with the observed decrease of $f_{\mathbf{A}}$ for closer spaced rings in experiment and simulation. This suggests that H_y may be overestimated and may not be significant in the ring structure. H_y is strong in saturated rings only in the hard-axis arms, away from the regions of maximum amplitude of mode **A**, and it will be smaller than the model as the moments bend around the perimeter of the ring.

Considering instead the contribution of H_x (~118 Oe) in modifying the demagnetizing factors, it is expected to decrease the resonance frequency by 280 MHz. This matches the experimental result for $\Delta f_{\mathbf{A}}$ for a rectangular ring in experiment, though it is twice that of the simulation. These calculations suggest that H_x is the major factor contributing to the decrease in $f_{\mathbf{A}}$ as s is reduced. Furthermore, the curvature of the circular ring increases the average spacing between rings and leads to a smaller influence of H_x on $f_{\mathbf{A}}$ for circular rings; hence smaller $\Delta f_{\mathbf{A}}$ values were observed for all t.

2. *The effect of thickness*

Next, we consider the effect of increasing t on $f_{\mathbf{A}}$ and $\Delta f_{\mathbf{A}}$. As t increases, N_z decreases, while N_x and N_y will increase, changing $f_{\mathbf{A}}$. Based on the rectangular prism model of Aharoni, N_z decreases from 3.548π to 3.096π as t increases from 30 nm to 80 nm, while N_x increases from 0.424π to 0.849π and N_y increases from 0.028π to 0.055π. As such, there is a more

rapid increase of (N_x-N_y) than the decrease of (N_z-N_y), and the resonance frequency will increase. Indeed, by incorporating these parameters into (1) we obtained $\Delta f_{\mathbf{A}} = 1.805$ GHz, a value close to the experimental $\Delta f_{\mathbf{A}} = 2.199$ GHz. However, at $t > 100$ nm, the $f_{\mathbf{A}}$ decreased slightly for all s. This may be a result of nonuniform magnetization in a thick ferromagnetic film [19,46–48]. Chen *et al*. [46] suggested that the uniform mode ($k = 0$) of spin waves may be scattered into magnons ($k \neq 0$) by this locally nonuniform magnetization and cause the resonance frequency to shift.

Next, we analyze the effect of t on $\Delta f_{\mathbf{A}}$ as a result of changes in the demagnetizing factors. Thicker rings produce higher stray field H_x and a larger $\Delta f_{\mathbf{A}}$. However, $\Delta f_{\mathbf{A}}$ becomes smaller with further increase of t above 80 nm in experiments, possibly as a result of competition with increasing H_y (calculated as 513 Oe at $t = 120$ nm).

IV. CONCLUSION

The dynamic behaviors of rectangular and circular rings were compared. Four resonance modes were present in rectangular rings, while only two resonance modes were observed in circular rings. The additional modes in rectangular modes were attributed to edge modes and to resonance related to DWs, respectively. The experimental results are described based on the Kittel formulation and an analytical stray field model. The frequency $f_{\mathbf{A}}$ of the highest intensity mode **A** was investigated at saturation as a function of spacing s and thickness t. $f_{\mathbf{A}}$ decreased as s was reduced for all t, which was attributed to changes in the stray field H_x. For the thickest rings, the stray field H_y apparently becomes significant and competes with H_x and lowers $\Delta f_{\mathbf{A}}$. Micromagnetic simulation results are in good agreement with the experiments.

These rings arrays provide a model structure to study the effect of shape anisotropy and dynamic interactions in modifying high-frequency response in structures such as magnonic crystals. The high-frequency response in these structures as a function of s and t may be useful in the design of a broadband high-frequency tunable filter [49,50]. For example, we have shown that by varying s and t, one can achieve a broadband frequency response. Furthermore, by varying the shape of the ring, one can tune the strength of dynamic coupling between neighboring rings. These results may be helpful in the development of DW logic, memory, and magnonic devices.

ACKNOWLEDGMENT

The support of the Singapore-MIT Alliance and SMF-NUS New Horizon Award is gratefully acknowledged.

[1] K. Yamada, S. Kasai, Y. Nakatani, K. Kobayashi, H. Kohno, A. Thiaville, and T. Ono, Nat. Mater. **6**, 270 (2007).
[2] S. Bohlens, B. Kruger, A. Drews, M. Bolte, G. Meier, and D. Pfannkuche, Appl. Phys. Lett. **93**, 142508 (2008).
[3] M. P. Kostylev, A. A. Serga, T. Schneider, B. Leven, and B. Hillebrands, Appl. Phys. Lett. **87**, 153501 (2005).
[4] T. Schneider, A. A. Serga, B. Leven, B. Hillebrands, R. L. Stamps, and M. P. Kostylev, Appl. Phys. Lett. **92**, 022505 (2008).
[5] J. Ding, M. Kostylev, and A. O. Adeyeye, Appl. Phys. Lett. **100**, 073114 (2012).
[6] A. B. Ustinov and B. A. Kalinikos, Appl. Phys. Lett. **90**, 252510 (2007).
[7] Z. K. Wang, V. L. Zhang, H. S. Lim, S. C. Ng, M. H. Kuok, S. Jain, and A. O. Adeyeye, ACS Nano **4**, 643 (2010).
[8] C. A. F. Vaz, T. J. Hayward, J. Llandro, F. Schackert, D. Morecroft, J. A. C. Bland, M. Kläui, M. Laufenberg, D. Backes, U. Rüdiger, F. J. Castaño, C. A. Ross, L. J. Heyderman, F. Nolting, A. Locatelli, G. Faini, S. Cherifi, and W. Wernsdorfer, J. Phys.: Condens. Matter **19**, 255207 (2007).
[9] C. A. Ross, F. J. Castaño, D. Morecroft, W. Jung, H. I. Smith, T. A. Moore, T. J. Hayward, J. A. C. Bland, T. J. Bromwich, and A. K. Petford-Long, J. Appl. Phys. **99**, 08S501 (2006).
[10] F. J. Castaño, D. Morecroft, and C. A. Ross, Phys. Rev. B **74**, 224401 (2006).
[11] L. J. Chang, C. Yu, T. W. Chiang, K. W. Cheng, W. T. Chiu, S. F. Lee, Y. Liou, and Y. D. Yao, J. Appl. Phys. **103**, 07C514 (2008).
[12] A. Imre, E. Varga, L. Ji, B. Ilic, V. Metlushko, G. Csaba, A. Orlov, G. H. Bernstein, and W. Porod, IEEE Trans. Magn. **42**, 3641 (2006).
[13] P. Vavassori, O. Donzelli, M. Grimsditch, V. Metlushko, and B. Ilic, J. Appl. Phys. **101**, 023902 (2007).
[14] P. Vavassori, M. Grimsditch, V. Novosad, V. Metlushko, and B. Ilic, J. Appl. Phys. **93**, 7900 (2003).
[15] X. Zhu, P. Grutter, V. Metlushko, and B. Ilic, J. Appl. Phys. **93**, 7059 (2003).
[16] M. D. Mascaro, H. S. Körner, C. Nam, B. G. Ng, and C. A. Ross, Appl. Phys. Lett. **98**, 252506 (2011).
[17] A. O. Adeyeye, S. Goolaup, N. Singh, C. C. Wang, X. S. Gao, C. A. Ross, W. Jung, and F. J. Castaño, J. Phys. D **40**, 6479 (2007).
[18] A. O. Adeyeye, N. Singh, and S. Goolaup, J. Appl. Phys. **98**, 094301 (2005).
[19] G. Shimon, A. O. Adeyeye, and C. A. Ross, J. Appl. Phys. **111**, 013909 (2012).
[20] X. H. Wang, W. K. Peng, and W. S. Lew, J. Appl. Phys. **106**, 043905 (2009).
[21] M. Kläui, C. A. F. Vaz, L. Lopez-Diaz, and J. A. C. Bland, J. Phys.: Condens. Matter **15**, R985 (2003).
[22] Y. G. Yoo, M. Kläui, C. A. F. Vaz, L. J. Heyderman, and J. A. C. Bland, Appl. Phys. Lett. **82**, 2470 (2003).
[23] C. Yu, T. W. Chiang, Y. S. Chen, K. W. Cheng, D. C. Chen, S. F. Lee, Y. Liou, J. H. Hsu, and Y. D. Yao, Appl. Phys. Lett. **94**, 233103 (2009).
[24] J. Wang, A. O. Adeyeye, and N. Singh, Appl. Phys. Lett. **87**, 262508 (2005).
[25] Y. Ren, S. Jain, A. O. Adeyeye, and C. A. Ross, New J. Phys. **12**, 093003 (2010).
[26] C. Nam, M. D. Mascaro, and C. A. Ross, Appl. Phys. Lett. **97**, 012505 (2010).
[27] P. Vavassori, D. Bisero, V. Bonanni, A. Busato, M. Grimsditch, K. M. Lebecki, V. Metlushko, and B. Ilic, Phys. Rev. B **78**, 174403 (2008).

[28] X. S. Gao, A. O. Adeyeye, and C. A. Ross, J. Appl. Phys. **103**, 063906 (2008).
[29] M. Kläui, C. A. F. Vaz, J. Rothman, J. A. C. Bland, W. Wernsdorfer, G. Faini, and E. Cambril, Phys. Rev. Lett. **90**, 097202 (2003).
[30] F. Giesen, J. Podbielski, T. Korn, and D. Grundler, J. Appl. Phys. **97**, 10A712 (2005).
[31] W. Xu, D. B. Watkins, L. E. DeLong, K. Rivkin, J. B. Ketterson, and V. V. Metlushko, J. Appl. Phys. **95**, 6645 (2004).
[32] I. Neudecker, M. Kläui, K. Perzlmaier, D. Backes, L. J. Heyderman, C. A. F. Vaz, J. A. C. Bland, U. Rüdiger, and C. H. Back, Phys. Rev. Lett. **96**, 057207 (2006).
[33] G. Gubbiotti, M. Madami, S. Tacchi, G. Carlotti, H. Tanigawa, T. Ono, L. Giovannini, F. Montoncello, and F. Nizzoli, Phys. Rev. Lett. **97**, 247203 (2006).
[34] F. S. Ma, V. L. Zhang, Z. K. Wang, H. S. Lim, S. C. Ng, M. H. Kuok, Y. Ren, and A. O. Adeyeye, J. Appl. Phys. **108**, 053909 (2010).
[35] J. Ding, M. Kostylev, and A. O. Adeyeye, Appl. Phys. Lett. **100**, 062401 (2012).
[36] H. Schultheiss, S. Schäfer, P. Candeloro, B. Leven, B. Hillebrands, and A. N. Slavin, Phys. Rev. Lett. **100**, 047204 (2008).
[37] K. Vogt, H. Schultheiss, S. Jain, J. E. Pearson, A. Hoffmann, S. D. Bader, and B. Hillebrands, Appl. Phys. Lett. **101**, 042410 (2012).
[38] T. Taniyama, I. Nakatani, T. Yakabe, and Y. Yamazaki, Appl. Phys. Lett. **76**, 613 (2000).
[39] V. E. Demidov, S. O. Demokritov, K. Rott, P. Krzysteczko, and G. Reiss, Appl. Phys. Lett. **92**, 232503 (2008).
[40] A. O. Adeyeye and N. Singh, J. Phys. D **41**, 153001 (2008).
[41] M. R. Scheinfein and E. A. Price, LLG Micromagnetics Simulator, software for micromagnetic simulations.
[42] F. Giesen, J. Podbielski, B. Botters, and D. Grundler, Phys. Rev. B **75**, 184428 (2007).
[43] E. M. Hempe, M. Kläui, T. Kasama, D. Backes, F. Junginger, S. Krzyk, L. J. Heyderman, R. Dunin-Borkowski, and U. Rüdiger, Physica Status Solidi (A) **204**, 3922 (2007).
[44] J. Norpoth, S. Dreyer, and J. Ch, J. Phys. D **41**, 025001 (2008).
[45] A. Aharoni, J. Appl. Phys. **83**, 3432 (1998).
[46] Y.-C. Chen, D.-S. Hung, Y.-D. Yao, S.-F. Lee, H.-P. Ji, and C. Yu, J. Appl. Phys. **101**, 09C104 (2007).
[47] E. J. Torok, A. L. Olson, and H. N. Oredson, J. Appl. Phys. **36**, 1394 (1965).
[48] D. D. Tang and Y.-J. Lee, *Magnetic Memory: Fundamentals and Technology* (Cambridge University Press, New York, 2010).
[49] N. N. Phuoc, F. Xu, and C. K. Ong, Appl. Phys. Lett. **94**, 092505 (2009).
[50] G. Gubbiotti, S. Tacchi, M. Madami, G. Carlotti, A. O. Adeyeye, and M. Kostylev, J. Phys. D **43**, 264003 (2010).